



AFRL-RX-WP-TP-2008-4354

**MODELING OF TEXTURE EVOLUTION DURING HOT
FORGING OF ALPHA/BETA TITANIUM ALLOYS
(PREPRINT)**

M.G. Glavicic, R.L. Goetz, D.R. Barker, G. Shen, D. Furrer, A. Woodfield, and S.L. Semiatin

Metals Branch

Metals, Ceramics, and NDE Division

JUNE 2007

Approved for public release; distribution unlimited.

See additional restrictions described on inside pages

STINFO COPY

**AIR FORCE RESEARCH LABORATORY
MATERIALS AND MANUFACTURING DIRECTORATE
WRIGHT-PATTERSON AIR FORCE BASE, OH 45433-7750
AIR FORCE MATERIEL COMMAND
UNITED STATES AIR FORCE**

REPORT DOCUMENTATION PAGE				<i>Form Approved</i> OMB No. 0704-0188	
<p>The public reporting burden for this collection of information is estimated to average 1 hour per response, including the time for reviewing instructions, searching existing data sources, gathering and maintaining the data needed, and completing and reviewing the collection of information. Send comments regarding this burden estimate or any other aspect of this collection of information, including suggestions for reducing this burden, to Department of Defense, Washington Headquarters Services, Directorate for Information Operations and Reports (0704-0188), 1215 Jefferson Davis Highway, Suite 1204, Arlington, VA 22202-4302. Respondents should be aware that notwithstanding any other provision of law, no person shall be subject to any penalty for failing to comply with a collection of information if it does not display a currently valid OMB control number. PLEASE DO NOT RETURN YOUR FORM TO THE ABOVE ADDRESS.</p>					
1. REPORT DATE (DD-MM-YY) June 2007		2. REPORT TYPE Journal Article Preprint		3. DATES COVERED (From - To)	
4. TITLE AND SUBTITLE MODELING OF TEXTURE EVOLUTION DURING HOT FORGING OF ALPHA/BETA TITANIUM ALLOYS (PREPRINT)				5a. CONTRACT NUMBER In-house	
				5b. GRANT NUMBER	
				5c. PROGRAM ELEMENT NUMBER 62102F	
6. AUTHOR(S) M.G. Glavicic, R.L. Goetz, and D.R. Barker (UES, Inc.) G. Shen and D. Furrer (Rolls-Royce Corporation) A. Woodfield (General Electric Aviation) S.L. Semiatin (AFRL/RXLMP)				5d. PROJECT NUMBER 4347	
				5e. TASK NUMBER RG	
				5f. WORK UNIT NUMBER M02R2000	
7. PERFORMING ORGANIZATION NAME(S) AND ADDRESS(ES) UES, Inc. ----- Rolls-Royce Corporation ----- General Electric Aviation				8. PERFORMING ORGANIZATION REPORT NUMBER AFRL-RX-WP-TP-2008-4354	
9. SPONSORING/MONITORING AGENCY NAME(S) AND ADDRESS(ES) Air Force Research Laboratory Materials and Manufacturing Directorate Wright-Patterson Air Force Base, OH 45433-7750 Air Force Materiel Command United States Air Force				10. SPONSORING/MONITORING AGENCY ACRONYM(S) AFRL/RXLMP	
				11. SPONSORING/MONITORING AGENCY REPORT NUMBER(S) AFRL-RX-WP-TP-2008-4354	
12. DISTRIBUTION/AVAILABILITY STATEMENT Approved for public release; distribution unlimited.					
13. SUPPLEMENTARY NOTES Journal article submitted to <i>Metallurgical and Materials Transactions A</i> . PAO Case Number: AFRL/WS 07-1466; Clearance Date: 20 Jun 2007. The U.S. Government is joint author of this work and has the right to use, modify, reproduce, release, perform, display, or disclose the work.					
14. ABSTRACT Texture development during the subtransus hot forging of alpha/beta titanium alloys with an equiaxed-alpha microstructure was modeled using the Los Alamos Polycrystalline Plasticity (LApp) code and <111> pencil-glide polycrystalline plasticity code coupled with the finite-element-method (FEM) program DEFORM. The methodology treated the partitioning of the imposed strain between the alpha and beta phases, and thus enabled the prediction of the distinct deformation textures developed in the primary alpha and beta matrix during hot working. Two variant selection rules in conjunction with the beta deformation texture were also examined to establish a method for predicting the transformation texture of secondary alpha developed as a result of beta decomposition during cool-down following forging or heat treatment. The approach was validated via an industrial-scale trail comprising hot pancake forging of Ti-6Al-4V.					
15. SUBJECT TERMS titanium, texture, modeling, strain partitioning, variant selection					
16. SECURITY CLASSIFICATION OF:			17. LIMITATION OF ABSTRACT: SAR	18. NUMBER OF PAGES 30	19a. NAME OF RESPONSIBLE PERSON (Monitor) Sheldon L. Semiatin 19b. TELEPHONE NUMBER (Include Area Code) N/A
a. REPORT Unclassified	b. ABSTRACT Unclassified	c. THIS PAGE Unclassified			

Modeling of Texture Evolution during Hot Forging of Alpha/Beta Titanium Alloys

M.G. Glavicic^{*}, R.L. Goetz^{*}, D.R. Barker^{*}, G. Shen^{**},
D. Furrer^{**}, A. Woodfield^{***}, and S.L. Semiatin
Air Force Research Laboratory, Materials and Manufacturing Directorate,
AFRL/MLLM, Wright-Patterson AFB, OH 45433-7817
^{*}UES, Inc., 4401 Dayton-Xenia Road, Dayton, OH 45432
^{**}Rolls-Royce Corporation, P.O. Box 420, Indianapolis, IN 46206-0420
^{***}General Electric Aviation, Cincinnati, OH 45215

Abstract

Texture development during the subtransus hot forging of alpha/beta titanium alloys with an equiaxed-alpha microstructure was modeled using the Los Alamos Polycrystalline Plasticity (LApp) code and a $\langle 111 \rangle$ *pencil-glide* polycrystalline plasticity code coupled with the finite-element-method (FEM) program DEFORMTM. The methodology treated the partitioning of the imposed strain between the alpha and beta phases, and thus enabled the prediction of the distinct deformation textures developed in the primary alpha and beta matrix *during* hot working. Two variant selection rules in conjunction with the beta deformation texture were also examined to establish a method for predicting the transformation texture of secondary alpha developed as a result of beta decomposition during cool-down following forging or heat treatment. The approach was validated via an industrial-scale trial comprising hot pancake forging of Ti-6Al-4V.

Keywords: Titanium, Texture, Modeling, Strain Partitioning, Variant Selection

1. Introduction

The modeling of texture evolution during the hot working of two-phase, alpha/beta titanium alloys with a microstructure of equiaxed (primary) alpha in a matrix of beta is complicated by several factors. First, the flow stress behaviors of the hexagonal-close-packed (hcp) alpha phase and the body-centered-cubic (bcc) beta phase differ and exhibit different dependences on temperature. Such differences result in an unequal partitioning of the imposed strain that drives the formation of *deformation* texture. Second, the beta phase decomposes to form secondary (platelet) alpha during cooling from the hot working (or final heat treatment) temperature. At moderate cooling rates, this phase transformation follows a Burgers-type orientation relationship,

$$\begin{aligned} \{110\}_{\beta} // (0001)_{\alpha} \\ \langle 111 \rangle_{\beta} // [2\bar{1}\bar{1}0]_{\alpha} \end{aligned} \quad (1)$$

in which there are twelve distinct possible variants that can form from a single orientation of a prior beta-phase grain; i.e., the secondary-alpha orientation is related to one of six $\{110\}_{\beta}$ planes, each of which contains two $\langle 111 \rangle_{\beta}$ directions. In addition, the *transformation* texture thus formed can vary widely depending upon the initial texture of the beta-phase and any predisposition for one or several of the twelve variants to form preferentially over the others.

The objective of the present work was to develop a modeling framework to describe the evolution of deformation and transformation texture during the thermomechanical processing of alpha/beta titanium alloys at temperatures in the two-

phase field. For this purpose, numerical techniques to describe strain partitioning and the crystal rotations associated with metal flow and crystal plasticity (i.e., slip) were integrated in a user-friendly manner and validated using an industrial-scale forging of Ti-6Al-4V.

2. Background

A brief review of pertinent previous efforts in the area of texture modeling is presented below to provide a background for the methodology used in the present work.

2.1 Texture Modeling

Several types of models can be used to predict the evolution of crystallographic texture during the large strain deformation of polycrystalline materials. These include the Sachs *isostress* approach [1], the Taylor *isostrain* model [2], and various crystal plasticity finite-element-method (CPFEM) codes. The Taylor model, which enforces strain compatibility between grains, generally provides the best balance between simplicity and accuracy. It forms the basis for the widely-used Los Alamos Polycrystalline Plasticity (LApp) code [3], which can be used to establish the evolution of crystallographic texture in *single-phase* metals during rolling, forging, extrusion, etc. However, the Taylor approach does not allow for strain variations from grain-to-grain, let alone within individual grains. When such non-uniformity is important, viscoplastic CPFEM models [4-6] are applied, but require substantial computer resources and are significantly more complex to apply to the large-strain deformation involved in an actual forging process. Recently, the program ALAMEL [7] was developed in an attempt to reduce computation requirements; it was applied to model texture evolution during the rolling of interstitial-free steel. In other work, Lebensohn and Canova [8] developed a viscoplastic self-consistent model to describe texture evolution in alpha/beta titanium alloys with a colony-alpha microstructure. Subsequently, this approach was validated for the simple compression and rolling of the two-phase Fe-Cu system by Commentz, et al. [9]. Although each of these models shows promise, neither is yet suitable for quantifying texture evolution during the hot forging of complex two-phase alloys in an industrial environment.

2.2 Modeling of Metal Flow during Forging

Rigid, viscoplastic FEM codes, such as DEFORM™ [10], are now used commonly in the forging industry. Such software has been applied to a variety of non-steady and steady-state processes to predict the effect of material properties, die design, and process variables on metal flow and the occurrence of defects. Typically, the workpiece material is assumed to be an isotropic continuum (i.e., with a random texture) whose deformation behavior is described by the von Mises criterion and associated flow rule. As a consequence, the development of crystallographic texture is not taken into account, let alone the effect of such texture evolution on the metal flow itself.

2.3 Coupled Metal Flow-Texture Models

To simplify the problem associated with describing metal flow and texture evolution during large-strain deformation, several research efforts have sought to couple continuum FEM and crystal-plasticity codes. Pérocheau, et al. [11] coupled an FEM

code with a polycrystalline plasticity model based upon the relaxed-constraints (RC) Taylor hypothesis to model the extrusion and rolling of fcc metals. Schoenfeld, et al. [12], modeled the through-thickness rolling textures of aluminum by including advanced friction and internal-variable constitutive models into a 2D FEM model developed by Lee, et al. [13]. More recently, the ALAMEL model [7], a statistical-type method with Taylor type homogenization, was used to model the texture developed in rolled interstitial-free steel.

3. Modeling Approach

In a similar fashion to the previous efforts of Van Houtte, et al., Pérocheau, et al., and Schoenfeld, et al. [7, 11, 12] on single-phase alloys, the present work to analyze texture evolution during the hot forging of two-phase alpha/beta titanium alloys, used a two dimensional FEM program to analyze crystal rotations due to metal flow and two Taylor *isostrain* models (Los Alamos Polycrystalline Plasticity (LApp) code [3] for the alpha phase and a $\langle 111 \rangle$ *pencil-glide* polycrystalline plasticity code for the beta phase) to quantify rotations due to crystal plasticity. The distinguishing features of the present work related to the treatment of strain partitioning between the phases and its effect on deformation texture evolution, the description of transformation texture and variant selection rules, and the integration of the software packages.

3.1 Self-Consistent Model of Strain Partitioning

The flow stresses of the individual phases in alpha/beta titanium alloys such as Ti-6Al-4V are very different at the temperatures typically used during hot forging, i.e., 800°C to 975°C. The alpha phase is approximately three times as strong as the beta phase [14]. In addition, the volume fraction of the phases varies greatly. For example, the volume fraction of alpha varies from ~80 pct. at 800°C to ~20 pct. at 975°C. Hence, the strain accommodated by the alpha and beta phases is not equal and may be expected to vary with temperature. Thus, an analytical method to quantify the strain accommodated by each phase is required to model the texture change associated with crystal plasticity. In the present work, a simple self-consistent approach [14] was adopted. This method is based on the technique developed by Hill [15] and later extended by Suquet [16] for linearly-elastic solids. Hill's analysis assumed that both phases are linearly viscoplastic; i.e., they each have a constitutive relation of the form:

$$\sigma_i = k_i^L \dot{\varepsilon}_i, \quad (2)$$

in which σ and $\dot{\varepsilon}$ denote the flow stress and strain rate, respectively, k^L is the “viscosity” coefficient, and the subscripts ($i = 1, 2$) refer to phases 1 or 2. The viscosity of the aggregate k_{sc}^L (which relates the aggregate flow stress and strain rate) is given by the following expression:

$$k_{sc}^L/k_1^L = (1/6) \left\{ 3 - 2\rho + 5(1-f)(\rho-1) + \sqrt{[3 - 2\rho + 5(1-f)(\rho-1)]^2 + 24\rho} \right\}, \quad (3)$$

in which $\rho = k_2^L/k_1^L$, and f denotes the volume fraction of phase 1.

Suquet [16] extended the above analysis to the case in which both phases are power-law viscoplastic, viz.,

$$\sigma_i = k_i \dot{\varepsilon}_i^{m_i}, \quad (4)$$

and the strain-rate sensitivity exponents for both phases are equal; i.e., $m_1 = m_2 = m$. In this case, the viscosity-like parameter of the aggregate (k) is a function of the values of viscosity-like parameters for the two phases, k_1 and k_2 , as well as m , ρ , and k_{sc}^L/k_1^L :

$$k/k_1 = \frac{\min}{\rho \geq 0} \left\{ \left(k_{sc}^L/k_1^L \right)^{(m+1)/2} \left[f + (1-f)\rho^{(m+1)/(m-1)} \left(k_2/k_1 \right)^{2/(1-m)} \right]^{(1-m)/2} \right\}, \quad (5)$$

In Equation (5), the expression on the right-hand side before the argument in braces denotes the minimum value for $\rho \geq 0$. In practice, the value of k_{sc}^L/k_1^L for the corresponding linearly-viscous case is unknown. Thus, the evaluation of k/k_1 involves a procedure in which trial values of ρ are guessed, k_{sc}^L/k_1^L , is determined from Equation (3), and ρ and k_{sc}^L/k_1^L are inserted into Equation (5). The value of ρ that yields the minimum value of k/k_1 is the appropriate one.

The *average* strain rates in the two phases are readily calculated from the values of k , k_1 , k_2 , and the volume fraction f of phase “1”. Following Hill [17], the aggregate flow stress σ_{ov} and strain rate $\dot{\epsilon}_{ov}$ are volume averages of the corresponding flow stresses and strain rates in the individual phases:

$$\sigma_{ov} = k \dot{\epsilon}_{ov}^m = f k_1 \dot{\epsilon}_1^m + (1-f) k_2 \dot{\epsilon}_2^m, \quad (6)$$

$$\dot{\epsilon}_{ov} = f \dot{\epsilon}_1 + (1-f) \dot{\epsilon}_2, \quad (7)$$

Solving Equation (7) for $\dot{\epsilon}_2$ as a function of $\dot{\epsilon}_{ov}$ and $\dot{\epsilon}_1$,

$$\dot{\epsilon}_2 / \dot{\epsilon}_{ov} = [1-f(\dot{\epsilon}_1 / \dot{\epsilon}_{ov})] / (1-f). \quad (8)$$

Inserting this relation into Equation (6), an expression for $\dot{\epsilon}_1 / \dot{\epsilon}_{ov}$ is obtained:

$$k/k_1 = f \left(\dot{\epsilon}_1 / \dot{\epsilon}_{ov} \right)^m + \left[(1-f)^{(1-m)} \left(k_2/k_1 \right) \left(1-f \left(\dot{\epsilon}_1 / \dot{\epsilon}_{ov} \right) \right)^m \right]. \quad (9)$$

Equation (9) cannot be solved analytically, but is readily evaluated using numerical techniques.

From Equations (8) and (9), the strain rates and hence strain increments for each phase are determined as a function of their relative flow stresses and volume fractions. The strain increments so determined were used in crystal-plasticity-model calculations to estimate rotations due to slip.

3.2 Beta-Phase Decomposition

At relatively slow cooling rates following hot forging (or heat treatment) of titanium components (i.e., $< 20^\circ\text{C}/\text{min}$), primary alpha particles grow epitaxially, consuming the majority of the beta matrix [8]. At faster cooling rates (between ~ 20 and $200^\circ\text{C}/\text{min}$), typical of fan cooling or water quenching of finite-section-size workpieces, the beta matrix decomposes at a critical supersaturation to form colonies of secondary-alpha platelets [18] each of which possess a Burgers-orientation relation with its parent beta matrix (Equation (1)).

The texture associated with the secondary-alpha phase can vary greatly depending on which of the twelve possible variants is selected during beta-phase decomposition.

The manner in which a beta phase orientation is transformed is governed by the relationship

$$D S_k^\beta B = A, \quad (10)$$

in which D is a rotation matrix, defined by the Euler angles $\varphi_1 = 135$, $\Phi = 90$, $\varphi_2 = 325$ [19], S_k^β is a subset of the cubic symmetry operators (Table 1), B is the beta phase orientation matrix, and A is the alpha phase orientation matrix.

In the present work, the secondary alpha of interest was formed during rapid cooling following solution treatment of a forging high in the alpha-beta phase field. Two different variant-selection possibilities were examined. These rules were based on the previous experimental observations for commercial-purity titanium [20-22] and Ti-6Al-4V [23-25].

In the first case, all variants were assumed to be equally likely. In this instance, a specific rotation matrix S_k^β from Table 1 was randomly selected from the twelve possibilities for the transformation of each individual beta phase orientation.

In the second case, $\langle 111 \rangle$ *pencil-glide* in the beta phase during cooling from the final solution heat treatment was assumed to control variant selection. Here, the methodology developed by Morris and Semiatin [26] was used to determine the $\langle 111 \rangle$ slip directions and slip planes activated to accommodate the strain increments developed during cooling, as predicted by FEM analysis. From the two closest $\{110\}$ planes that could have equivalently accommodated this same shear strain via $\langle 111 \rangle$ *pencil-glide* [see Figure 4 in reference 34], the $\{110\}\langle 111 \rangle$ slip system on which the highest resolved shear stress had been developed was assumed to comprise the plane/direction that determined the orientation of the selected alpha variant. Because the variants of the alpha phase are assumed to form per the Burgers relationship (Equation (1)), the resolved shear stress τ on a given $\{110\}\langle 111 \rangle$ slip system in the beta phase for a given imposed stress state will be the same as the resolved shear stress on the $(0001)[2\bar{1}\bar{1}0]$ slip system in the alpha phase after the phase transformation. The equivalent slip planes/directions of the beta and alpha phase are then related by

$$\tau = m_\beta^{(s)} : B \sigma B^T = m_\alpha^{basal\langle a \rangle} : A \sigma A^T, \quad (11)$$

in which $m_\beta^{(s)}$ and $m_\alpha^{basal\langle a \rangle}$ are the tensor quantities $m_{ij}^{(s)} = \frac{1}{2}[\hat{b}_i \hat{n}_j + \hat{b}_j \hat{n}_i]$, in which the slip direction \hat{b} , and slip plane normal \hat{n} are defined by $\{110\}\langle 111 \rangle$ slip systems of the beta phase and the $(0001)[2\bar{1}\bar{1}0]$ slip system of the alpha phase. Inserting Equation (10) into Equation (11)

$$m_\beta^{(s)} : B \sigma B^T = m_\alpha^{basal\langle a \rangle} : D S_k^\beta B \sigma (D S_k^\beta B)^T, \quad (12)$$

permits the specific alpha phase variant $D S_k^\beta B$ that has the same resolved shear stress as in the beta phase to be selected from the 12 possible variants and used to transform the beta phase orientation.

3.3 Calculation Procedures and Integration of Software Packages

Current crystal-plasticity FEM codes are too demanding from a computational standpoint to model texture evolution at every material point during the forging of a single-phase alloy, let alone for a complex forging of a two-phase material. Thus, the

present work consisted of a decoupled approach in which crystal rotations due to metal flow and crystallographic slip were treated separately, thereby providing a compromise between scientific rigor and user-friendliness in an industrial environment. To this end, the FEM metal-flow program DEFORM™ and the two crystal-plasticity codes (LApp [3] and the <111> pencil-glide model of Morris and Semiatin [26]) were selected. In addition to these software packages, other specially-developed codes were incorporated into a series of user-friendly GUIs that could be easily operated.

Model calculations consisted of running DEFORM™ in the usual manner. After the DEFORM™ simulation was run, the strain increments and *metal-flow-related* rotation for each time step and FEM node (integration point) was output in the form of a set of ASCII files. The strain increments were partitioned per the approach described in Section 3.1 and used as input to separate alpha-phase and beta-phase calculations of the slip-related rotations. For the alpha-phase, LApp [3] was used to model the texture evolution, whereas for the beta phase, the Morris and Semiatin <111> *pencil-glide* approach [26] was used. The crystal plasticity input also included experimental pole-figure data (from x-ray or neutron diffraction or EBSD measurements) obtained using the Los Alamos Preferred Orientation Package (popLA) [3] and other internally developed software. After each strain increment, the texture change (equal to the sum of the metal-flow and LApp/<111> *pencil-glide* calculated, slip-related rotations) was imposed at each node for each phase. The resulting texture was then used as the initial texture for the next increment of deformation.

Subsequent to the crystal plasticity calculations, an additional FEM simulation was performed to model the quenching procedure that followed the final heat treatment of a pancake forging used as the validation example. The predicted beta-phase texture was then converted to a secondary-alpha texture using each of the two possible variant-selection rules using the stresses and strains predicted to have been developed at the median temperature (~810 °C) at which secondary alpha would have been expected to nucleate during quenching [27]. The predicted primary-alpha (deformation) texture and secondary-alpha (transformation) texture were then weighted per the relative volume fractions of the phases and added to obtain the overall alpha-phase texture. The volume fraction of primary alpha is function of the forging temperature and the cooling rate; it can be estimated using a simple diffusion analysis [18, 27]. The volume fraction of secondary alpha was then taken to be the difference between the total alpha content (typically of the order of 0.95 for alloys such as Ti-6Al-4V) and the primary-alpha volume fraction. Alternatively, EBSD techniques, such as that described by Germain, et al. [28], can be used to separate the primary- and secondary-alpha constituents.

4. Materials and Experimental Procedures

The texture developed during the final heat treatment of a Ti-6Al-4V pancake forging was used to validate the modeling approach described in Section 3.

4.1 Material

The validation material comprised a 280-mm diameter Ti-6Al-4V billet whose composition (in weight percent) was 6.62 aluminum, 4.10 vanadium, 0.19 oxygen, 0.007 nitrogen, 0.02 carbon, 0.004 hydrogen, balance titanium. The initial microstructure of the

billet material at the forging preheat temperature (955°C) consisted of equiaxed, primary-alpha particles in a matrix of the beta phase (Fig. 1).

The variation of the volume fraction of beta with temperature (the so-called beta-approach curve), which was needed for both the strain-partitioning calculations and the determination of the overall alpha-phase texture, was determined using PANDAT™ [29] and its associated titanium database. The beta-approach curve between 700°C and the beta-transus temperature (~995°C) was fit to a seventh-order polynomial function.

4.2 Experimental Procedures

The validation trial comprised the hot-die forging of a cylindrical billet whose initial dimensions were 280-mm diameter x 510-mm height. The preform was coated with glass, preheated at 955°C, and forged to a 70-pct. height reduction between flat tool-steel dies preheated to approximately 600°C to minimize workpiece chilling. Forging was conducted in a hydraulic press at a constant crosshead speed to produce a nominal strain rate of 0.7 s⁻¹. With the prescribed die and billet temperatures and deformation rate, it was estimated that the preform temperature remained between 870 and 955°C and that deformation heating at the center of the preform did not play a significant role. Immediately following forging, the pancake was water quenched. Subsequently, the forging was given a final heat treatment at a temperature 30°C below the beta transus for one hour and water quenched.

The forging and quenching operations were modeled using DEFORM™. The point-tracking feature within the software was used to identify the local strain increments, metal-flow rotation, and cooling transients (during water quenching) at six specific locations within the pancake (Figures 2 and 3).

Specimens extracted from the pancake forging at the six tracking-point locations were metallographically prepared for microstructural characterization and texture measurement. The microstructures were characterized using a Leica Stereoscan 360 FE scanning-electron microscope (SEM). The textures in the final forging, as well as at the corresponding locations in the starting billet, were quantified using x-ray diffraction to establish (10 $\bar{1}$ 0), (0002), (10 $\bar{1}$ 1), (10 $\bar{1}$ 2), and (11 $\bar{2}$ 0) alpha-phase pole figures and (110) and (200) beta-phase pole figures. The pole figures were measured in the Schultz-reflection mode using Cu K α radiation. Analysis of the measured data was performed using popLA. The input to crystal-plasticity codes for the deformation-texture simulations consisted of the initial textures and slip modes. To model the evolution of texture in the primary-alpha phase, LApp [3] was used and deformation was assumed to be possible via basal <a>, prism <a>, and pyramidal <c+a> slip with a ratio of the corresponding critical-resolved shear stresses of 1, 0.7, and 3, respectively. For the beta phase, deformation via <111> *pencil-glide* was modeled using the methodology of Morris and Semiatin [26].

In order to gage the accuracy of the modeling capability for the alpha-phase *deformation* texture alone, a specimen from the RT location in the forging was taken to the final heat treatment temperature and then furnace cooled to produce a structure that was essentially fully equiaxed alpha. Pole figure measurements for this sample were made in the same manner as the other samples.

5. Results and Discussion

5.1 Microstructure Observations

Following the final heat treatment, a variety of bimodal microstructures was developed in the forging (Fig. 4). The different microstructures can be ascribed to the variation in local cooling rate (Fig. 3), the supersaturations that were developed, and the temperature at which the secondary alpha was formed [18]. At the bore-midplane location (BC, Fig. 4a), for example, a bimodal microstructure of equiaxed alpha in a transformed matrix of coarse, colony (secondary) alpha was formed. The microstructure was similar at the top of the bore (location BT, Fig. 4c), despite the somewhat faster cooling rate at BT compared to that at BC (Fig. 3). At the rim-midplane location (RC, Fig. 4b), the secondary alpha was somewhat finer even though the cooling rate here (Fig. 3) was estimated to be between that of the bore-midplane and bore-top locations. A much finer microstructure was formed at the rim-top region (RT, Fig. 4d); higher magnification micrographs revealed that the secondary alpha here had a basketweave morphology whose formation could be explained by the very fast cooling rate, deduced from the FEM simulations (Fig. 3). In general, the variation of the volume fraction of primary alpha with location (Table 2) corresponded to the cooling rate; i.e., slower cooling rates led to a greater tendency for epitaxial growth of primary alpha and hence a greater final fraction of this constituent. On the other hand, a more detailed analysis appears to be needed to explain the details of the formation and thickening of secondary-alpha plates.

5.2 Texture Measurements and Model Predictions

The texture developed in the pancake forging also varied from location to location. At the BC location (Fig. 5a) and other locations along the axis of the pancake, an axisymmetric texture was formed for the primary + secondary alpha phases. The textures predicted using the FEM stresses and strain increments developed at 810 °C (Fig. 6) showed that specific features in the measured pole figures could be explained with the variant selection rules chosen (Fig 5b and Fig 5c).

In the case for which all variants were considered possible (Fig. 5b), a pole appeared at the 6 and 12 o'clock positions in the $(11\bar{2}0)$ pole figure and a fiber along the horizontal equatorial plane of the (0002) pole figure. Moreover, fiber textures above and below the horizontal equatorial planes of the (0002) and $(11\bar{2}0)$ pole figures were also predicted. These features were also observed in the measured pole figures (Fig. 5a).

For the $\langle 111 \rangle$ *pencil-glide* variant-selection approach, which allowed several variants to form from a single beta orientation (Fig 5c) the fiber textures above and below the horizontal equatorial planes of the (0002) and $(11\bar{2}0)$ pole figures were more pronounced. Moreover, two strong poles appeared diagonally in the (0002) and $(11\bar{2}0)$ pole figures. The corresponding measured pole figures (Fig. 5a) also showed poles at these locations, suggesting possibly that slip system activity may influence which variants will form. This result is similar to that found in the work of Gey, et al. [24], who were able to correlate alpha-variant selection following rolling in the beta phase field to the most active $\{110\} \langle 111 \rangle$ and $\{211\} \langle 111 \rangle$ slip systems. However, the lack of predicted poles at the 6 and 12 o'clock positions in the predicted $(11\bar{2}0)$ pole figure

indicates that this variant-selection approach can not explain a number of the features observed in the measured pole figures (Fig. 5a).

A (0002) fiber-texture component, as seen by the poles at the 12 and 6 o'clock positions in the (0002) pole figure and the maximum along the horizontal equatorial plane in the (11 $\bar{2}$ 0) pole figure, was also predicted using both variant selection rules (Fig 5b and Fig 5c). Unfortunately, these types of texture components were not observed in the experimental data (Fig 5a). Hence, further work is required to ascertain the origins of this texture component.

At other locations in the pancake forging for which there was significant rotation due to metal flow, such as RT, a more complex texture was formed (Fig. 7a). The stresses and strain increments developed at this location (Fig. 8) were dissimilar to those developed at the BC location (Fig. 6). Using the stresses and strains developed at 810 °C and the variant selection rules based on $\langle 111 \rangle$ *pencil-glide* activity, model predictions (Fig 7c) did not successfully predict the majority of the features in the measured pole figures (Fig. 7a). When all variants were considered possible (Fig 7b), a marked improvement in the correlation was observed. This result is consistent with the microstructure (Fig. 4d) present at this location, in that somewhat random nucleation and growth of the alpha phase would have been expected to have occurred in the production of the observed basketweave microstructure.

The cooling rate experienced at the RT location was sufficient to produce the orthorhombic (α'') martensitic phase in addition to the secondary-alpha platelets. Based on the lattice parameters of α'' ($a = 3.033$, $b = 4.924$, and $c = 4.667$ Å) deduced in previous x-ray diffraction work [30, 31], four of the five measured pole figures ((10 $\bar{1}$ 0), (0002), (10 $\bar{1}$ 1), and (11 $\bar{2}$ 0)) for the primary + secondary alpha phase were confounded by the α'' martensitic phase due to diffraction-peak overlap. Moreover, the α'' martensitic phase has a

$$\begin{aligned} (110)_\beta // (001)_{\alpha''} \\ [111]_\beta // [101]_{\alpha''} \end{aligned} \quad (13)$$

orientation relationship with the β -phase [32, 33], with perhaps its own set of variant-selection criteria for the 12 possible variants. Thus the α'' martensitic phase will be textured in some manner related to the texture of the β -phase and may have some effect even at relatively low volume fractions on the calculated orientation distribution function (ODF) and the recalculated pole figures for the primary + secondary alpha at the RT location (Fig. 7a).

From a quantitative perspective, the model predictions of the alpha-phase texture *intensity* for all locations were reasonably close in some cases and high in others for the variant-selection rules examined. At the BC location (i.e., Fig. 5), the predicted texture using all variants (Fig 5b) was comparable to the measured texture (Fig 5a), whereas the modeled texture using the $\langle 111 \rangle$ *pencil-glide* activity (Fig 5c) was 4 to 5 times that which was measured. At the RT location, the predicted texture strength using all variants (Fig. 7b) was comparable to the measurement (Fig. 7a). These findings can be rationalized in part due to the fact that Taylor-type models typically predict textures that are *stronger* than those measured. Hence in regions such as location BC, where a large amount of strain is accommodated (Table 2), an over-prediction in the texture is to be

expected and will be compounded by the use of any type of variant-selection biasing criterion that limits which variants form (Fig 5b). In addition, the number of discrete orientations which were automatically generated to represent the initial billet texture of the alpha and beta phase in the present work (~1000) was insufficient to fully populate the orientation space. As a result, similar to a coarse grain specimen whose texture is measured using x-ray diffraction, the simulated pole figures were spotty, thus limiting the ability to make quantitative texture predictions.

Other differences in the measured-versus-predicted pole figures of a quantitative nature may be attributable to the rapid spatial variation in the cooling profiles in specimens close to the outer extremities of the forging. In specimens close to the pancake outer surface, such as the RT specimen, the modeled stresses, cooling rates, and microstructures varied significantly over the surface of the specimen in spite of the large initial billet and final pancake forging dimensions. Moreover, the modeled cooling rates and observed changes in the microstructures developed were consistent with the formation of a low volume fraction of the textured α' martensitic phase, which would also contribute to the observed quantitative differences in the pole figures.

For specimens at the interior of the pancake forging, such as the BC location, cooling-rate gradients were present, but to a much smaller degree. As a result, the microstructures were relatively homogeneous over the entire sample surface, and the gradients were concluded to play a minor role in the differences in the intensities of the various components of the measured and predicted pole figures.

A comparison of the measured textures for RT samples that were solution treated and furnace cooled (Fig. 9a) (to retain solely the equiaxed alpha phase and its associated deformation texture) or water quenched (Fig. 7a) showed significant differences, thus illustrating the contribution of the transformation texture to the overall alpha-phase texture. Furthermore, the deformation-texture prediction for the furnace-cooled RT sample showed qualitative agreement with the measurement (Figure 9a versus Figure 9b), but the texture intensity was again approximately twice as strong. Because a Taylor-type crystal plasticity model was used, such a result was again not unexpected.

6. Summary and Conclusions

The development of crystallographic texture during the forging and heat treatment of two-phase (alpha/beta) titanium alloys has been modeled by coupling software to treat strain partitioning between the phases, crystal rotations due to metal flow and slip, and variant selection during the decomposition of beta to form secondary (platelet) alpha. The method was evaluated using an industrial-scale Ti-6Al-4V pancake forging. A comparison of measured and predicted textures showed qualitative and in some cases quantitative agreement. However, several refinements are needed such as improvement in the deformation texture model to reduce the tendency for over-prediction of texture intensity and methods to account for possibly competitive variant-selection mechanisms.

Acknowledgements

This work was conducted as part of the in-house research of the Metals Processing Group in the Air Force Research Laboratory, Materials and Manufacturing Directorate. The support of the laboratory management and the Air Force Office of Scientific Research (Dr. J.S. Tiley, program manager) are gratefully acknowledged. This

project was motivated by the Air Force Metals Affordability Initiative program on Microstructure and Mechanical Property Modeling for Wrought Titanium Alloys led by the Ladish Company (Cudahy, WI). All of the authors (except SLS) were supported under the auspices of Contract No. F33615-99-2-5215 (Project LAD-2). The authors would also like to thank J.D. Miller for experimental assistance.

References

1. Sachs, G., *Z. Verein. Deutch Ing.*, 1928, **72**, 734.
2. Taylor, G.I., *J. Int. Metals*, 1938, **62**, 307.
3. Los Alamos Polycrystal Plasticity Code, Los Alamos National Laboratory report LA-CC-88-6, Los Alamos, NM, 1988.
4. Barton, N.R., *Modeling Crystal Elasto-plastic and Misorientation Structure at the Sub-grain Scale*, Ph.D. thesis, Cornell University, 2001.
5. Marin, E.B. and Dawson, P.R., *Comput. Methods Appl. Mech Engrg.*, 1998, **165**, 23.
6. Prantil, V.C., Jenkins, J.T. and Dawson, P.R., *J. Mech. Phys. Solids*, 1995, **43**, 1283.
7. Van Houtte, P., Li, S., Seefeldt, M., and Delannay, L., *J. Plasticity*, 2005, **21**, 589.
8. Lebensohn, R.A. and Canova, G.R., *Acta Mater.*, 1997, **45**, 3687.
9. Commentz, B., Hartig, Ch. and Mecking, H., *Comp. Mat. Sci.*, 1999, **16**, 237.
10. DEFORM™ 2D, version 8.2, Scientific Forming Technologies Corporation, Columbus, OH, 2005.
11. Pérocheau, F. and Driver, J.H., *Int. J. of Plast.*, 2000, **16**, 73.
12. Schoenfeld, S.E. and Asaro, R.J., *Int. J. Mech. Sci.*, 1996, **38**, 661.
13. Lee, C.S. and Duggan, B.J., *Met. Trans.*, 1991, **22A**, 2637.
14. Semiatin, S.L., Montheillet, F., Shen, G., and Jonas, J.J., *Metall. Mater. Trans. A*, 2002, **33A**, 2719.
15. Hill, R., *J. Mech. Phys. Solids*, 1965, **13**, 213.
16. Suquet, P.M., *J. Mech. Phys. Solids*, 1993, **41**, 981.
17. Hill, R., *J. Mech. Phys. Solids*, 1967, **15**, 79.
18. Semiatin, S.L., Knisley, S.L., Fagin, P.N., Zhang, F., and Barker, D.R., *Metall. Mater. Trans.*, 2003, **34A**, 2377.
19. Glavicic, M.G., Kobryn, P.A., Bieler, T.R. and Semiatin, S.L., *Mat. Sci. Eng.*, 2003, **A346**, 50.
20. Zhu, Z.S., Gu, J.L. and Chen, N.P., *Scripta Mater.*, 1996, **34**, 1281.
21. Zhu, Z.S., Gu, J.L., Liu, R.Y., Chen, N.P., and Yan, M.G., *Mat. Sci. Eng.*, 2000, **A280**, 199.
22. Gey, N. and Humbert, M., *Acta Mater.*, 2002, **50**, 277.
23. Gey, N., Humbert, M., Philippe, M.J., and Combres, Y., *Mat. Sci. Eng.*, 1996, **A219**, 80.
24. Gey, N., Humbert, M., Philippe, M.J., and Combres, Y., *Mat. Sci. Eng.*, 1997, **A230**, 68.
25. Moustahfid, H., Humbert, M., and Philippe, M.J., *Acta Mater.*, 1997, **45**, 3785.
26. Morris, P.R. and Semiatin, S.L., *Texture of Cryst. Solids*, 1979, **3**, 113.
27. Miller, J.D. and Semiatin, S.L., *Metall. Mater. Trans.*, 2005, **36A**, 259.
28. Gemain, L., Gey, N., Humbert, M., Hazotte, A., Bocher, P., and Jahazi, M., *Mater. Character.*, 2005, **54**, 216.
29. PANDAT, Computherm LLC, Madison, WI, 2006.

30. Glavicic, M.G. and Semiatin, S.L., *Acta Mater.*, 2006, **54**, 5337.
31. Zeng, L, and Bieler, T.R., *Mater. Sci. Eng.*, 2005, **A392**, 403.
32. Duerig, T.W., Albrecht, J., Richter, D. and Fisher, P., *Acta Metall.*, 1982, **30**, 2161.
33. Pionnier, D., Humbert, M., Philippe, M.J., and Combres, Y., *Acta Mater.*, 1998, **46**, 5891.
34. Piehler, H.R., and Backofen, W.A., *Metall. Trans.*, 1971, **2**, 249.

Table 1. Subset of cubic symmetry operators used to transform the beta phase into distinct alpha phase variants

$S_1^\beta = \begin{bmatrix} 1 & 0 & 0 \\ 0 & 1 & 0 \\ 0 & 0 & 1 \end{bmatrix}$	$S_5^\beta = \begin{bmatrix} 0 & -1 & 0 \\ 0 & 0 & -1 \\ 1 & 0 & 0 \end{bmatrix}$	$S_9^\beta = \begin{bmatrix} 0 & 0 & 1 \\ -1 & 0 & 0 \\ 0 & -1 & 0 \end{bmatrix}$
$S_2^\beta = \begin{bmatrix} 0 & 0 & 1 \\ 1 & 0 & 0 \\ 0 & 1 & 0 \end{bmatrix}$	$S_6^\beta = \begin{bmatrix} 0 & 1 & 0 \\ 0 & 0 & -1 \\ -1 & 0 & 0 \end{bmatrix}$	$S_{10}^\beta = \begin{bmatrix} -1 & 0 & 0 \\ 0 & 1 & 0 \\ 0 & 0 & -1 \end{bmatrix}$
$S_3^\beta = \begin{bmatrix} 0 & 1 & 0 \\ 0 & 0 & 1 \\ 1 & 0 & 0 \end{bmatrix}$	$S_7^\beta = \begin{bmatrix} 0 & 0 & -1 \\ 1 & 0 & 0 \\ 0 & -1 & 0 \end{bmatrix}$	$S_{11}^\beta = \begin{bmatrix} -1 & 0 & 0 \\ 0 & -1 & 0 \\ 0 & 0 & 1 \end{bmatrix}$
$S_4^\beta = \begin{bmatrix} 0 & -1 & 0 \\ 0 & 0 & 1 \\ -1 & 0 & 0 \end{bmatrix}$	$S_8^\beta = \begin{bmatrix} 0 & 0 & -1 \\ -1 & 0 & 0 \\ 0 & 1 & 0 \end{bmatrix}$	$S_{12}^\beta = \begin{bmatrix} 1 & 0 & 0 \\ 0 & -1 & 0 \\ 0 & 0 & -1 \end{bmatrix}$

Table 2. Dependence of the volume fraction of primary alpha and effective strain on location in the pancake forging

Location	Volume Fraction of Primary Alpha (%)	Effective Strain
BC	46	2.635
MC	48	2.011
RC	42	1.266
BT	38	0.055
MT	39	0.599
RT	30	1.105

Figure Captions

- Fig. 1. Backscattered-electron image of microstructure developed in Ti-6Al-4V at 955°C followed by water quenching. The dark, equiaxed phase is primary alpha. The gray, transformed phase was beta at the heat-treatment temperature.
- Fig. 2. Specimens extracted from the Ti-6Al-4V pancake forging for microstructure and texture examination. BC: bore-midplane, MC: midradius-midplane, RC: rim-midplane, BT: bore-top, MT: midradius-top, and RT: rim-top locations.
- Fig. 3. FEM-model predictions of temperature transients at different locations in the pancake forging during quenching following final heat treatment.
- Fig. 4. Backscattered-electron images of microstructures developed in the Ti-6Al-4V pancake forging following water quenching from the final heat treatment at the (a) bore-midplane, (b) rim-midplane, (c) bore-top, and (d) rim-top locations.
- Fig. 5. Alpha-phase pole figures for the bore-midplane (BC) location following forging and heat treatment: (a) measured, (b) simulated with all variants, (c) simulated with preferential variant selection based on $\langle 111 \rangle$ *pencil-glide*.
- Fig. 6. FEM predictions at the bore-midplane (BC) location: (a) stress and (b) strain components and temperature as a function of time during water quenching following solution heat treatment of the forging.
- Fig. 7. Alpha-phase pole figures for the rim-top (RT) location following forging and heat treatment: (a) measured, (b) simulated with all variants, (c) simulated with preferential variant selection based on $\langle 111 \rangle$ *pencil-glide*.
- Fig. 8. FEM predictions at the rim-top (RT) location: (a) stress and (b) strain components and temperature as a function of time during water quenching following solution heat treatment of the forging.
- Fig. 9. Primary-alpha pole figures for the rim-top (RT) location following forging + solution heat treatment + furnace cooling: (a) measured and (b) simulated.

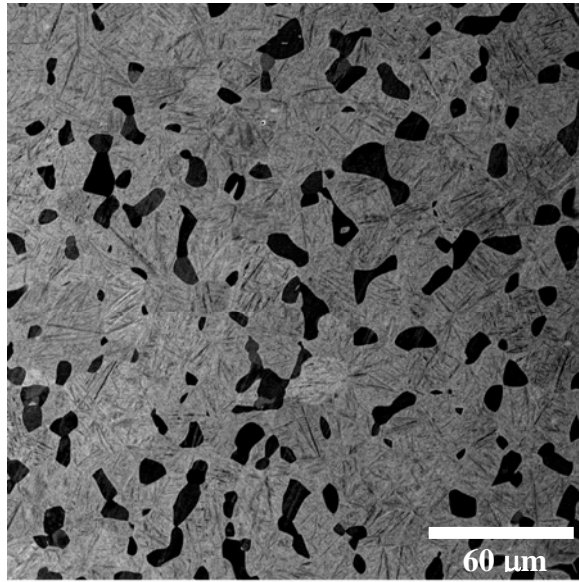


Figure 1

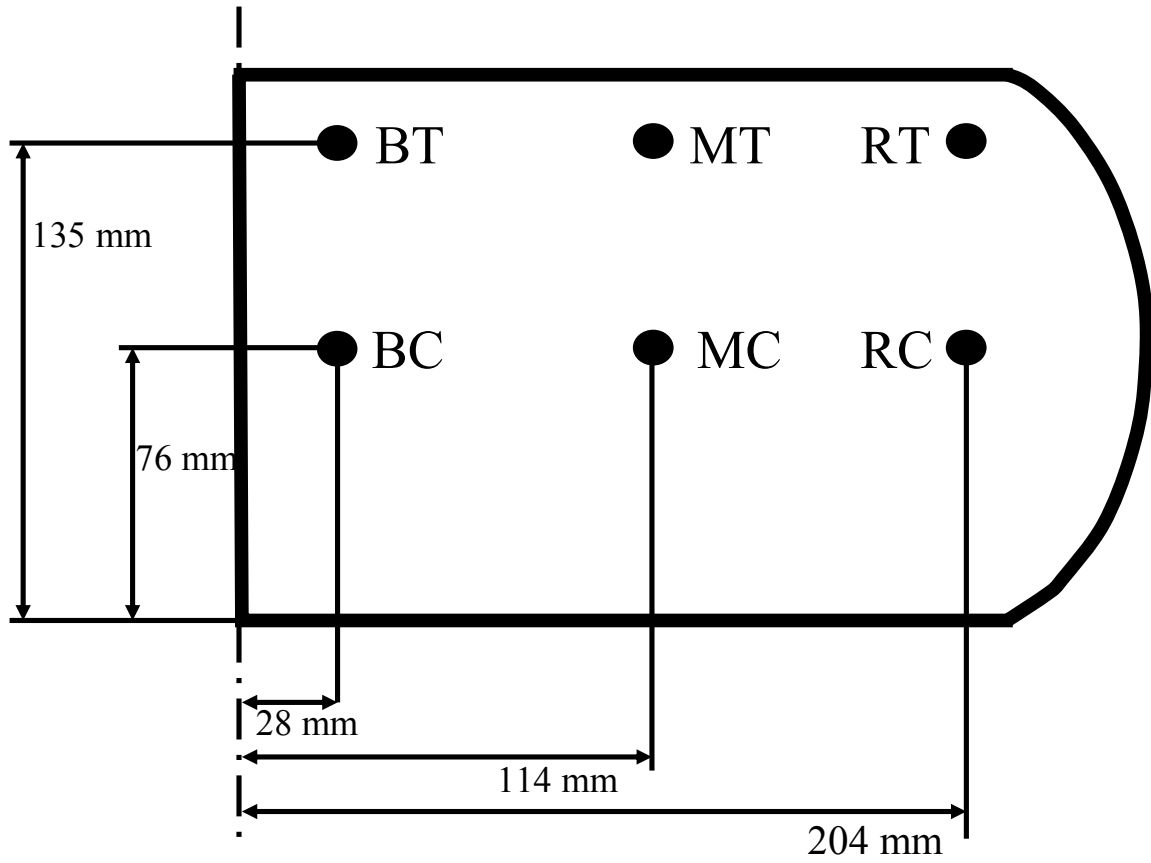


Figure 2

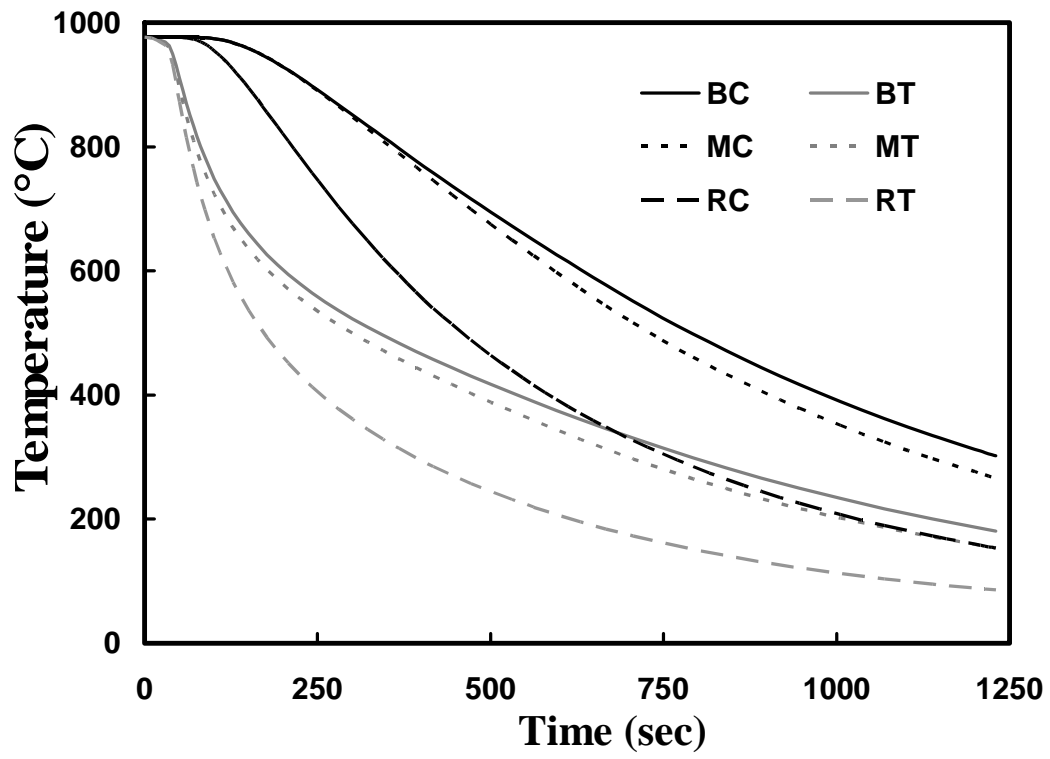


Figure 3

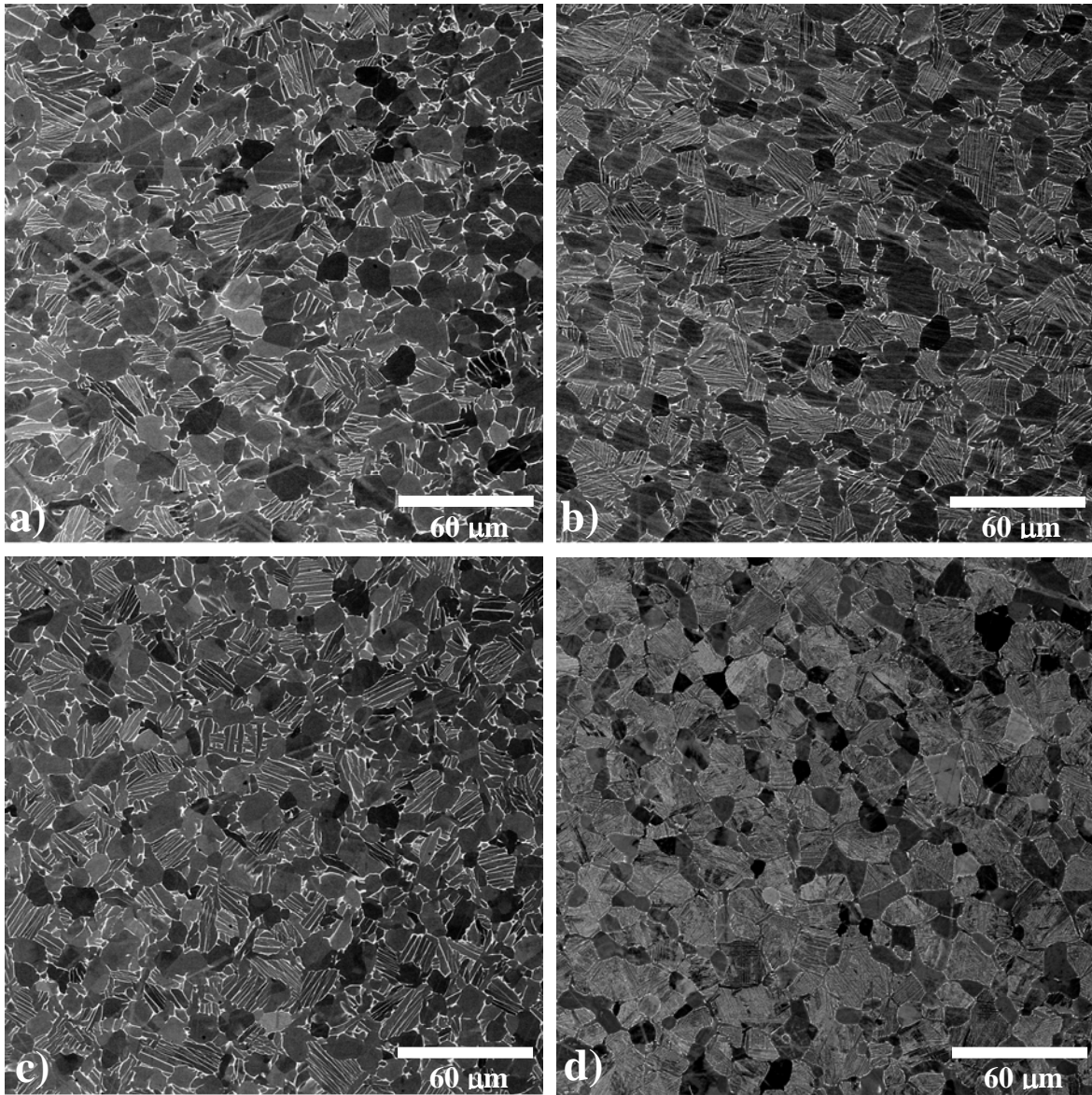


Figure 4

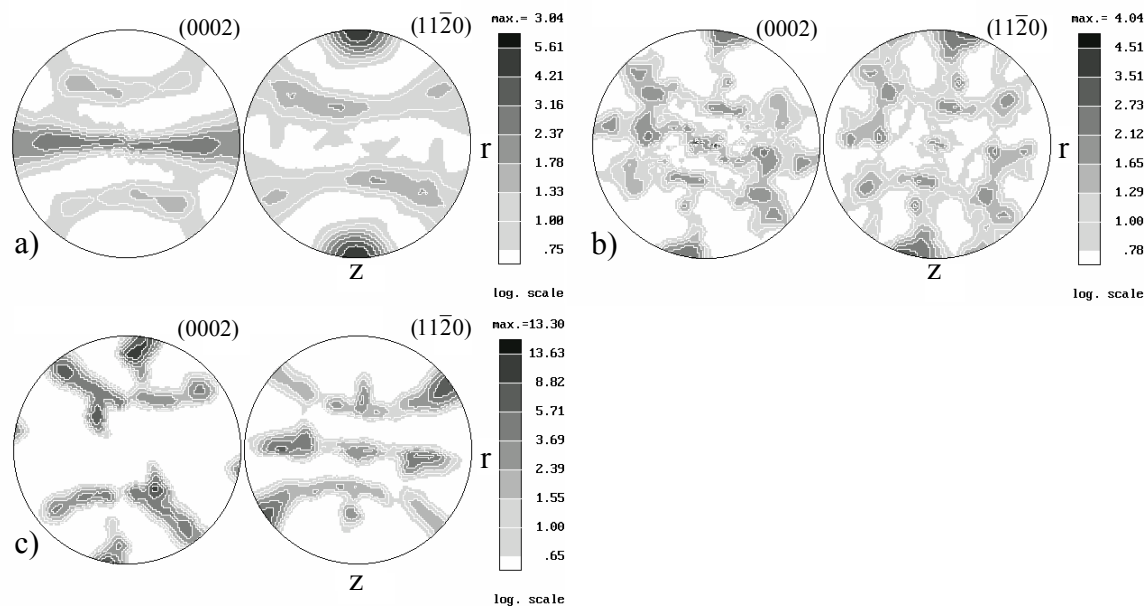
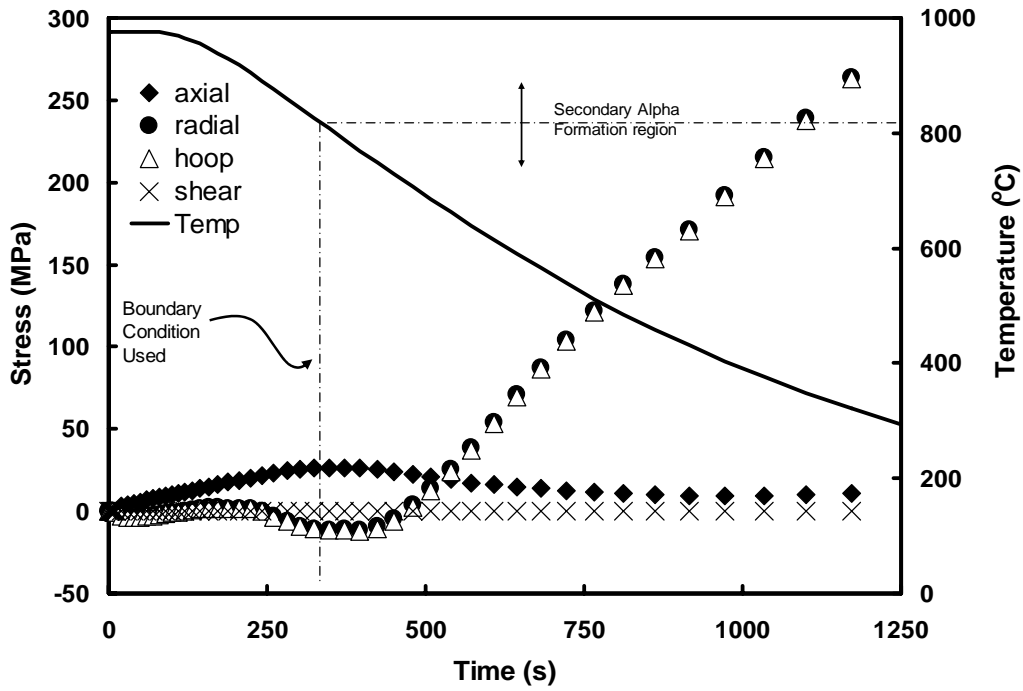
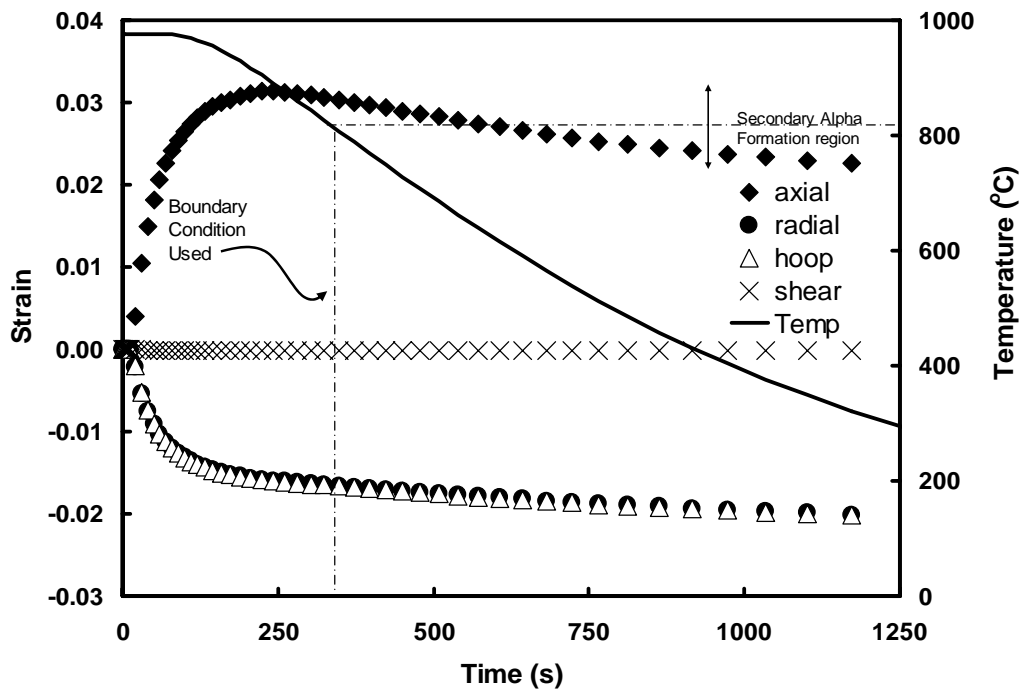


Figure 5



a)



b)

Figure 6 21

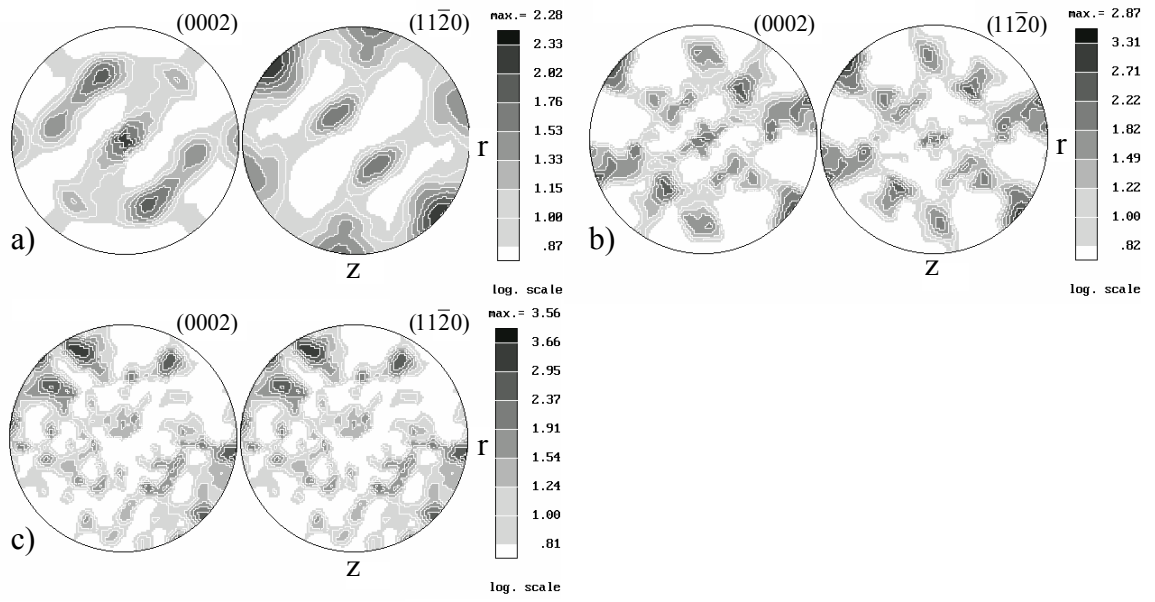
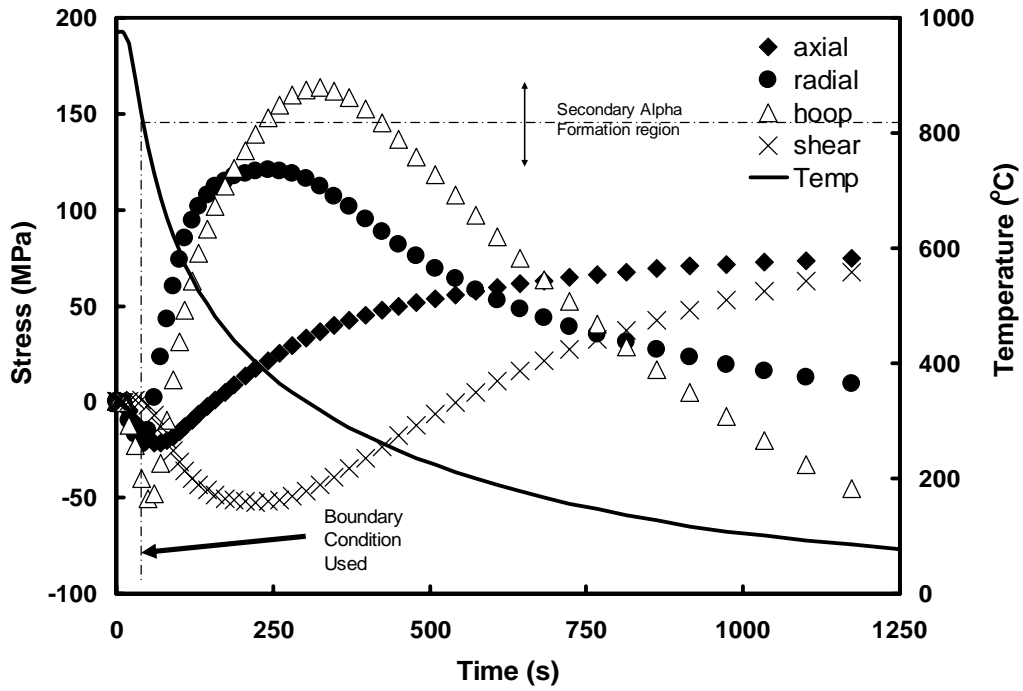
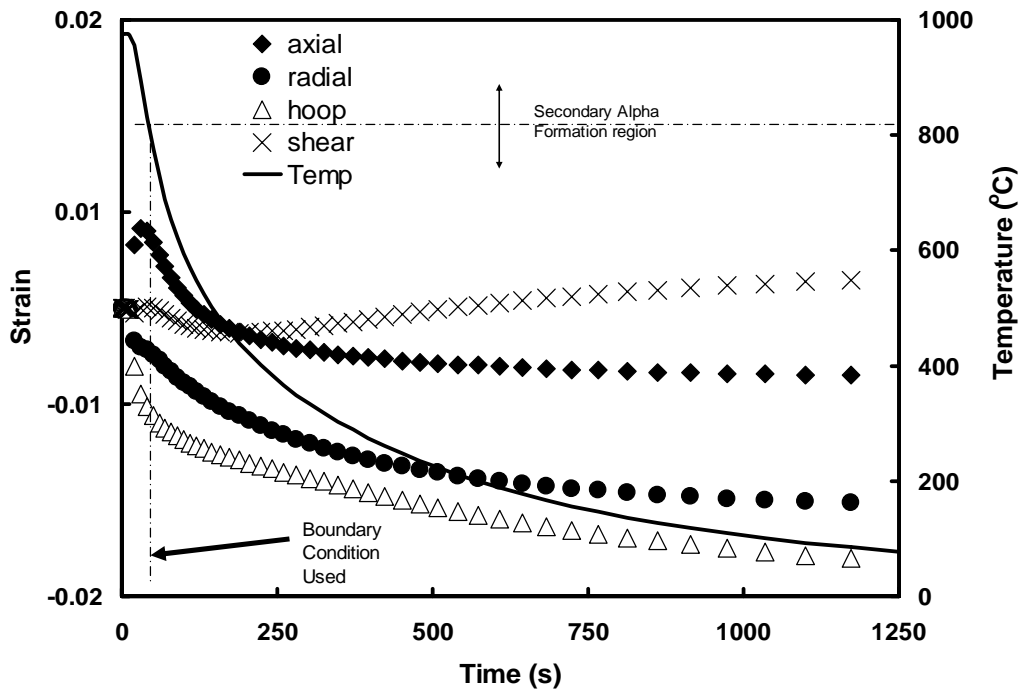


Figure 7



a)



b)

Figure 8 23

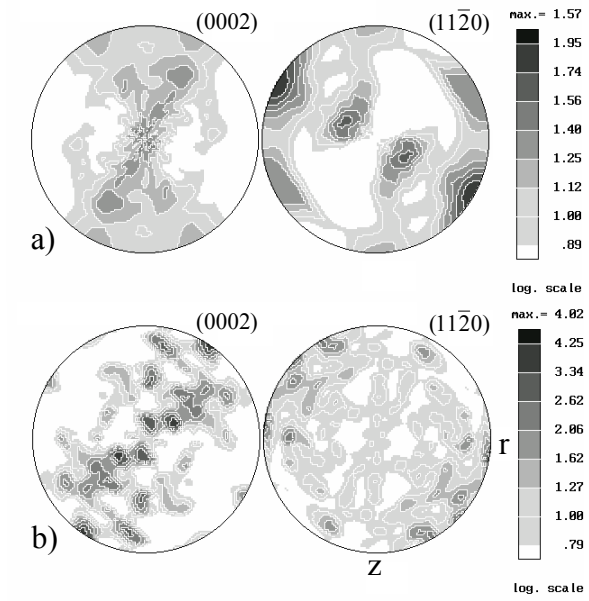


Figure 9